Climate and topography control the size and flux of sediment produced on steep mountain slopes

Clifford S. Riebe[a,1], Leonard S. Sklar[b], Claire E. Lukens[a], and David L. Shuster[c,d]

[a]Department of Geology and Geophysics, University of Wyoming, Laramie, WY 82071; [b]Department of Earth and Climate Sciences, San Francisco State University, San Francisco, CA 94132; [c]Department of Earth and Planetary Science, University of California, Berkeley, CA 94720; and [d]Berkeley Geochronology Center, Berkeley, CA 94709

Edited by Thomas Dunne, University of California, Santa Barbara, CA, and approved September 1, 2015 (received for review February 22, 2015)

Weathering on mountain slopes converts rock to sediment that erodes into channels and thus provides streams with tools for incision into bedrock. Both the size and flux of sediment from slopes can influence channel incision, making sediment production and erosion central to the interplay of climate and tectonics in landscape evolution. Although erosion rates are commonly measured using cosmogenic nuclides, there has been no complementary way to quantify how sediment size varies across slopes where the sediment is produced. Here we show how this limitation can be overcome using a combination of apatite helium ages and cosmogenic nuclides measured in multiple sizes of stream sediment. We applied the approach to a catchment underlain by granodiorite bedrock on the eastern flanks of the High Sierra, in California. Our results show that higher-elevation slopes, which are steeper, colder, and less vegetated, are producing coarser sediment that erodes faster into the channel network. This suggests that both the size and flux of sediment from slopes to channels are governed by altitudinal variations in climate, vegetation, and topography across the catchment. By quantifying spatial variations in the sizes of sediment produced by weathering, this analysis enables new understanding of sediment supply in feedbacks between climate, tectonics, and mountain landscape evolution.

weathering | erosion | critical zone | detrital thermochronometry

The interplay of climate and life drives weathering on mountain slopes (1–4), converting intact bedrock into mobile sediment particles ranging in size from clay to boulders (5, 6). Water, wind, and biota sweep these particles across slopes under the force of gravity and erode them into channels, where they serve as tools that cut into underlying bedrock during transport downstream (7). Both the size and flux of particles eroded from slopes into channels can influence incision into bedrock (8, 9), which in turn governs the pace of erosion from slopes where the sediment is produced (10, 11). The relationships between sediment production, hillslope erosion, and channel incision imply that they are central to feedbacks that drive mountain landscape evolution (12). When channel incision and hillslope erosion are relatively fast, sediment particles spend less time exposed to weathering on slopes (13) and thus may be coarser when they enter the channel (14), promoting faster incision into bedrock (7). Integrated over time, channel incision and hillslope erosion generate topography (15), imposing altitudinal gradients in precipitation, temperature, and hillslope form (16), and thus ultimately influencing erosion (17), weathering (1), and the sizes of sediment produced on slopes (2). Thus, the size and erosional flux of sediment may both depend on and regulate rates of channel incision into bedrock via feedbacks spanning a range of scales and processes.

Feedbacks between climate, erosion, and tectonics have been widely studied (8, 16, 18–23). However, understanding the role of sediment size remains a fundamental challenge (6–9, 12), due to a lack of methods for quantifying how the size distributions of sediment particles vary across the slopes where sediment is produced from bedrock by weathering and erosion (5, 6). Here we show how to overcome this limitation using a combination of tracing methods on multiple sediment sizes collected from streams in steep landscapes. Results from the Sierra Nevada, California, enable new understanding of connections between climate, mountain topography, and sediment supply.

Tracking Multiple Sediment Sizes in a Steep Catchment

Our approach exploits two widely used sediment tracing tools: detrital thermochronometry, which identifies the elevations of hillslopes where sediment was produced by weathering of underlying bedrock (24–27), and cosmogenic nuclides in stream sediment, which reflect the erosion rate of the sediment averaged over the hillslopes where particles in the sample were produced (28). Thus, whereas detrital thermochronometry can be used to quantify spatial variations in sediment production, cosmogenic nuclides in detrital minerals can be used to quantify spatially averaged erosion rates of sediment contributing areas.

Detrital thermochronometry is well illustrated at Inyo Creek, which drains the eastern flanks of the High Sierra (Fig. 1 and *SI Appendix*, Fig. S1). Across catchment slopes, apatite helium ages in bedrock increase with elevation (24), from ~20 My near the catchment mouth to ~70 My at the summit of Lone Pine Peak (Fig. 1, *SI Appendix*, and Dataset S1). Thus, sediment collected from the creek should have apatite helium ages that reveal the relative contributions of different elevations to the sediment flux at the sampling point (24). In the reference case of uniform sediment production and erosion, each point on the landscape is equally prone to producing a sediment particle and delivering it to the creek (29, 30). In that case, the measured age distribution

Significance

Rivers carve through landscapes using sediment produced on hillslopes by biological, chemical, and physical weathering of underlying bedrock. Both the size and supply rate of sediment influence the pace of river incision and landscape evolution, but the connections remain poorly understood, because the size distributions of sediment supplied from slopes have been difficult to quantify. This study combined existing sediment-tracing techniques in a previously unidentified approach to quantify sediment production across an alpine catchment in the High Sierra, California. Results show that colder, steeper, and less vegetated slopes produce coarser sediment that erodes faster into the channel network. These results demonstrate that the sediment-tracing approach can be used to quantify feedbacks between climate, topography, and erosion.

Author contributions: C.S.R., L.S.S., C.E.L., and D.L.S. designed research; C.S.R., L.S.S., C.E.L., and D.L.S. performed research; C.S.R., L.S.S., C.E.L., and D.L.S. contributed new reagents/analytic tools; C.S.R., L.S.S., C.E.L., and D.L.S. analyzed data; and C.S.R., L.S.S., and C.E.L. wrote the paper.

The authors declare no conflict of interest.

This article is a PNAS Direct Submission.

Freely available online through the PNAS open access option.

[1]To whom correspondence should be addressed. Email: criebe@uwyo.edu.

This article contains supporting information online at www.pnas.org/lookup/suppl/doi:10.1073/pnas.1503567112/-/DCSupplemental.

in creek bed sediment should be similar in shape to the age distribution in underlying bedrock (24–27, 29, 30), calculated by combining the catchment's elevation distribution with its age–elevation relationship (Fig. 1). Thus, any inconsistencies between the age distributions of sediment and bedrock delimit elevations that differ from the reference case of spatially uniform sediment production and delivery to the creek.

Cosmogenic nuclides serve as tracers of erosion because they accumulate in minerals in the uppermost few meters of rock and soil during exhumation to the landscape surface. Thus, the concentration of cosmogenic nuclides in eroded sediment reflects the erosion rate of the sediment. Slower erosion yields higher nuclide concentrations, because minerals spend more time near the surface interacting with cosmic radiation. Mixtures of minerals from areas with different erosion rates should reflect the spatially averaged erosion rate of the combined area, because each point on the landscape sheds minerals and thus nuclides in proportion to its erosion rate. Thus, minerals in sediment delivered to a creek should have an average nuclide concentration that reflects the average erosion rate of the sediment contributing area (28).

Although it has not been previously recognized in the literature, erosion rate information from cosmogenic nuclides in multiple sediment sizes can be combined with sediment source information from detrital thermochronometry to quantify altitudinal variations in both the erosion rate and the size distribution of sediment particles across a catchment. As a proof of concept, we used data from two sediment sizes sampled from Inyo Creek at a point where the contributing area spans roughly 2 km of relief (Fig. 1). Climate and topography vary substantially with altitude across the catchment, allowing us to test mechanistic hypotheses about chemical, physical, and biological factors that influence sediment production. From the lowest elevation at the catchment outlet to the highest at Lone Pine Peak, mean annual temperature decreases by nearly 12 °C, average precipitation increases by a factor of ~3, the prevalence of steep slopes increases markedly, and desert scrub and conifers give way to barren alpine slopes (Fig. 1). Thus, higher elevations are colder, steeper, and less vegetated than lower elevations. Meanwhile, the catchment has never been glaciated (24) and has three similar stocks of granodiorite bedrock (Dataset S2), thus minimizing the potentially confounding effects of glacial erosion and differences in lithology (31) in our study of climatic and topographic effects on sediment size and erosion rate.

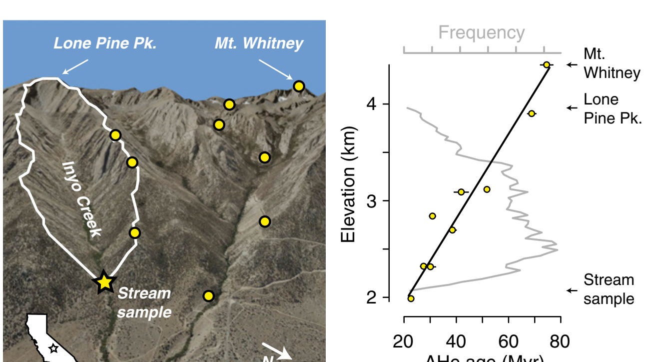

Fig. 1. Study site. (*Left*) Oblique view showing bedrock age locations (circles; after ref. 24), stream sediment sampling site (star), and catchment boundary. (*Right*) The relative frequency of elevation (gray line; top axis) from a 10-m DEM of the catchment plotted against elevation along with means (± SEM) of apatite helium (AHe) ages (circles; lower axis) for bedrock sampled from locations on *Left*. Line through data (*Right*) is least-squares, error-weighted regression of age against elevation.

The differences in climate, topography, and biota across the study catchment should drive altitudinal differences in chemical, biological, and physical weathering (1, 2, 4), which may, in turn, prompt spatial variations in both the size and flux of sediment eroded from slopes. We hypothesize that higher elevations are more strongly influenced by physical weathering and thus produce coarser sediment that erodes faster into the creek than lower elevations, where biological and chemical disaggregation of bedrock dominate. To test our hypothesis, we collected very coarse gravel (32–48 mm diameter) from Inyo Creek (Dataset S3) and measured apatite helium ages and cosmogenic ^{10}Be in minerals separated from the sediment (*SI Appendix* and Datasets S4 and S5). This enables comparisons with previously measured apatite helium ages and cosmogenic ^{10}Be (Datasets S5 and S6) from a sample of finer sediment (24).

Results

Spatial Variations in Sediment Size. By a variety of measures, the very coarse gravel has significantly older apatite helium ages than the finer sediment, indicating that it originated from higher in the catchment (Fig. 2 and *SI Appendix*, Fig. S2). Both a t test and a Mann–Whitney U test demonstrate that the gravel's apatite is older than finer sediment's apatite ($P = 0.0004$ and $P = 0.00003$, respectively). Statistically significant differences also emerge from Kolmogorov–Smirnov and Kuiper tests of the measured cumulative age distributions ($P = 0.0004$ and $P = 0.0023$, respectively; *SI Appendix* and Dataset S7). In addition, Hodges–Lehmann estimators show that paired differences in ages between the gravel and finer sediment have a statistically significant median of 6.3 My and a 95% confidence interval for differences in inferred source elevations of 149–404 m (median = 266 m). These differences are too large to be explained by any differences in the analytical procedures and sampling locations between this study and previous work (*SI Appendix*).

To explain the measured altitudinal differences in ages in terms of factors that might influence sediment production, we needed to first delimit the elevation ranges that exhibit exceedingly high and low production of gravel and finer sediment. Our benchmark for comparison was the range of plausible measured age distributions in our creek bed samples under the reference condition that each point on the landscape is equally likely to contribute clasts to the creek. We generated plausible distributions for this reference case of uniform erosion using standard bootstrapping methods—i.e., by randomly sampling the bedrock elevation distribution 73 and 52 times, to simulate measured age distributions of gravel and finer sediment, respectively. Each sampled elevation was assigned an age using the age–elevation relationship (Fig. 1), and results were collapsed into an age distribution for each simulation of spatially uniform sediment production and erosion (*SI Appendix*). Next, we repeated the simulations 30,000 times each and ranked the measured age distributions relative to the simulations at each elevation. Exceptionally low or high percentile ranks, below 2.5 or above 97.5, imply that the measured difference from the median of simulations is unlikely to have arisen by chance when all points on the landscape are contributing equally to sediment in the creek (Fig. 3 *A* and *B*). Thus, we identified elevations over which we can be 95% confident that the contributions of the different sizes of sediment are high or low compared with a random sample reflecting uniform sediment production and erosion across the catchment.

Our analysis indicates that the gravel is markedly underrepresented in the 2- to 2.35-km elevation band and overrepresented in the 2.6- to 2.75-km elevation band (Fig. 3*A*) relative to the case of uniform erosion. The difference is especially pronounced in the lower band: Although it accounts for ~15% of the catchment area, it produced just ~1% of the gravel we sampled from the creek (Fig. 2). Meanwhile, finer sediment is markedly overrepresented in the 2.45- to 2.55-km elevation band and underrepresented in the 3.1- to 3.5-km elevation band relative to

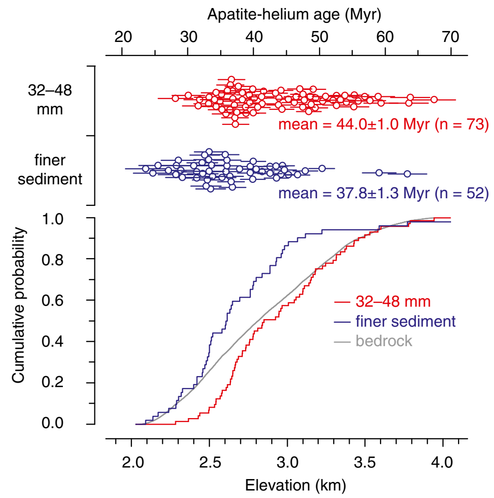

Fig. 2. Measured apatite helium ages and inferred erosional source elevations of sediment. (*Top*) Apatite helium ages (± propagated analytical error) and inferred source elevations for very coarse gravel with diameters of 32–48 mm (red circles) and finer sediment (blue circles; after ref. 24). Means (± SEM) are labeled along with n, the number of measurements. (*Bottom*) Cumulative age distributions (CADs, after ref. 25) for very coarse gravel (red line) and finer sediment (blue line). Gray line is CAD for catchment elevations from 10-m DEM (n = 33,900). Upper and lower axes are linked by the age–elevation relationship in Fig. 1.

the median of the simulations (Fig. 3*B*). For example, the upper 30% of the catchment produced just 10% of the sampled finer sediment (Fig. 2). Thus, our results suggest that production of the finer sediment is enhanced at lower elevations and inhibited at higher elevations (Fig. 3*B*). Overall, nearly half of the catchment's elevation range exhibits positive or negative departures that lie outside the 95% confidence interval of the uniform erosion simulations for either the gravel or finer sediment (Fig. 3). Thus, detrital thermochronometry reveals sharp contrasts in the erosional source elevations of the two sediment samples.

Spatial Variations in Erosion Rates. Measurements of cosmogenic nuclides reveal similarly sharp differences in the rates at which the different sizes of sediment have been shed from the slopes where they are produced to the sampling point in the channel. The cosmogenic ^{10}Be concentrations in quartz from the gravel and finer sediment are 1.01(±0.05) × 10^5 and 1.56(±0.01) × 10^5 atoms per gram, respectively (*SI Appendix* and Dataset S5). These results imply two markedly different spatially averaged erosion rates for the catchment, according to conventional methods for interpreting detrital ^{10}Be data (28). The discrepancy arises because the two sediment sizes represent erosion from different elevations of the catchment in different proportions (Fig. 2). Thus, the ^{10}Be results from Inyo Creek reveal a complication in interpreting cosmogenic nuclide data from sediment in steep landscapes: When eroded sediment size is spatially variable, any one size class of sediment considered in isolation can yield a distorted perspective on catchment-wide erosion rates. The discrepancies between the age distributions of the gravel and finer sediment (Fig. 2) show that similar errors can arise in studies of detrital thermochronometry (see also ref. 25).

We avoided some of the potential for misinterpretation of sediment tracing data by integrating the erosion rate information with the information on the sizes of sediment produced at different elevations. The ^{10}Be data show that hillslopes are eroding faster at elevations where the coarser sediment is dominantly produced. Meanwhile the apatite helium ages clearly show that the coarser sediment was eroded from higher elevations, on average, than the finer sediment (Fig. 2). Thus, we can interpret the ^{10}Be and apatite helium data together to indicate that erosion rates increase with elevation across the catchment. To quantify this relationship more precisely, we used an optimization algorithm to search for the altitudinal gradient in erosion rates that best matches the measured

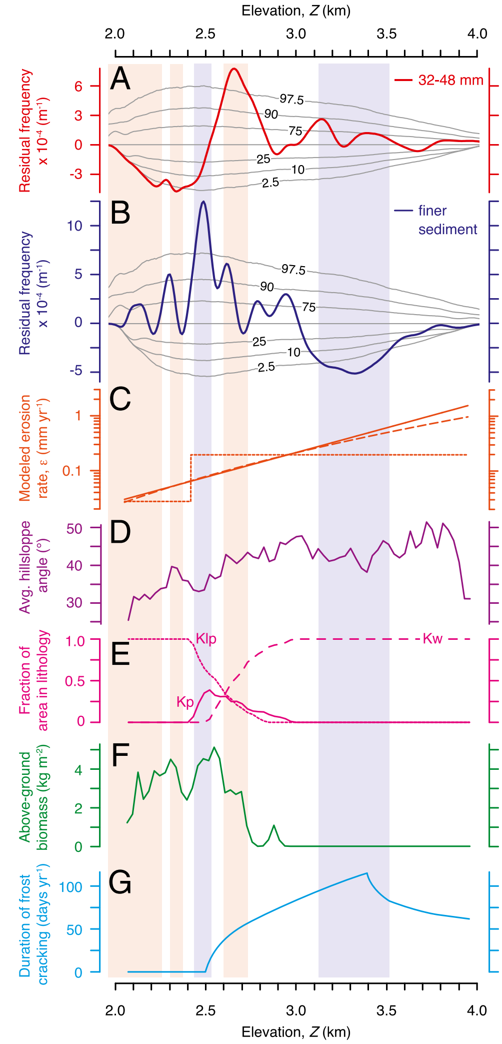

Fig. 3. Altitudinal variations in sediment production and driving factors (Dataset S8). Apatite helium ages of very coarse gravel (*A*) and finer sediment (*B*) expressed as differences between measured age distributions (see *SI Appendix*, Fig. S1) and median of 30,000 simulations of uniform erosion from the catchment. Labeled gray lines (*A* and *B*) show percentiles of departures from median for all simulations. Light blue and red vertical bands mark elevations over which measured age distributions (red and blue lines) lie outside the 95% confidence interval of the simulations. (*C*) Variations in erosion rate (ε, in millimeters per year) with elevation (*Z*, in kilometers) based on optimization of apatite helium and ^{10}Be data in very coarse gravel and finer sediment (see *SI Appendix*). Lines show best fits for exponential (solid: $\varepsilon = 0.2e^{2.1(Z-Z^*)}$, where Z^* = 2.96 km, a reference elevation), power-law [dashed: $\varepsilon = 0.2(Z/Z^*)^{5.5}$], and step-wise (dotted) functions. Best-fit linear function implies negative erosion for slopes near catchment mouth (an impossible scenario). Average hillslope angle (*D*) from 10-m DEM increases with elevation (r^2 = 0.39, P < 0.0001). (*E*) Fraction of landscape area at each elevation underlain by Lone Pine (Klp), Paradise (Kp), and Whitney (Kw) granodiorite. Biomass (*F*) is resampled at 10-m resolution from a 30-m remotely sensed dataset. (*G*) Number of days per year in frost-cracking window (with air temperature between −3 °C and −8 °C) inferred from modern temperature data (*SI Appendix*). Data in *D* and *F* were averaged in 30-m elevation bands.

^{10}Be concentrations. The approach employs a forward model that expresses the catchment as a collection of points with elevations extracted from a 10-m digital elevation model (DEM). The apatite helium ages allow us to specify the elevation distribution of sediment production for gravel and finer sediment (Fig. 2). We considered four functions for the altitudinal increase in erosion rates: linear, exponential, power, and step. The linear, exponential, and power functions each have two adjustable parameters (a slope and an intercept), and the step function has three (a higher value, a lower value, and an elevation where it changes). For each function, we adjusted the parameters incrementally, ran a forward model of sediment erosion for every parameter combination, and calculated a misfit for each model run as the sum of squared differences between predicted and observed ^{10}Be concentrations in the sediment (see *SI Appendix*). The parameter combination with the lowest misfit for each function was used to plot erosion rates versus elevation in Fig. 3*C*. The minimum misfits of the three functions are all similarly low. Moreover, without additional constraints from other sediment sizes, we cannot reliably identify which function agrees best with our observations. Nevertheless, the three best-fit functions in Fig. 3*C* exhibit a common pattern: Erosion rates increase markedly with altitude. For example, the exponential function shows a fiftyfold increase from ∼0.03 mm·y^{-1} at the bottom of the catchment to 1.5 mm·y^{-1} at the top.

Discussion

Our analysis of detrital thermochronometry and cosmogenic nuclides reveals that both the size and flux of sediment vary markedly across Inyo Creek slopes. The altitudinal increases in sediment size and erosion rates indicate that the catchment harbors considerable spatial variations in effectiveness of processes that break bedrock down and deliver it to channels. These variations likely arise due to altitudinal differences in topography and climate across the catchment.

Topography, Erosion Rates, and Sediment Size. Average hillslope angle increases with altitude across most of the catchment (Fig. 3*D*). Thus, the inferred altitudinal variations in erosion rates correlate strongly with topography for both the exponential and power-law functions (Fig. 4). These trends, together with the broad scatter in erosion rates at steep hillslope angles, match patterns observed in so-called threshold landscapes in previous studies of spatially averaged erosion rates from multiple catchments (17, 32, 33). Here they emerge from a single catchment, illustrating the power of using information from multiple sizes and multiple sediment tracing techniques to quantify spatial variations in the size and flux of sediment produced on slopes.

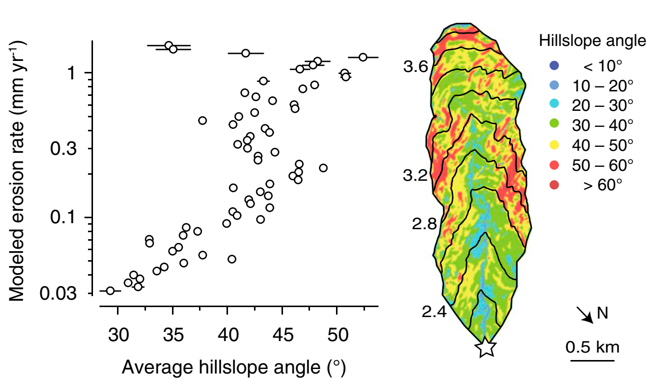

Fig. 4. Topographic control of erosion rates. (*Left*) Erosion rates from best-fit exponential function (Fig. 3*C*) increase with average hillslope angle. Erosion rates from best-fit power law (see Dataset S8) follow a similar, but less steep trend. (*Right*) Map showing distribution of hillslope angles from the 10-m DEM. Contour interval, 0.2 km. Star, sediment sampling site.

Erosional processes are evidently wearing away slopes in catchment headwaters much faster than slopes near the outlet (Fig. 3*C*). However, the trends quantified here reflect just a snapshot averaged over the 10^3- to 10^4-y timescales of the methods. Extrapolated over the last several million years, the inferred spatial variations in erosion rates imply substantial headward erosion of the catchment into the low-relief surface of the High Sierra (Fig. 1). In that case, the steepest slopes associated with the fastest erosion rates and coarsest sizes could have reached the modern catchment divide at Lone Pine Peak in just 2–4 My (*SI Appendix*), similar to the time elapsed since movement on the Sierra Nevada Frontal Fault accelerated base-level lowering of streams draining the range (34). This raises the possibility that the catchment itself (Fig. 1) and the altitudinal trends in sediment size and flux (Fig. 3) are all outcomes of a wave of differential erosion that has been propagating into the range since the Pliocene.

Connections between our results and the tectonics of the range are speculative, due to mismatches in timescale. However, the connections between topography and erosion rates are strong (Fig. 4). They are also consistent with our hypothesis about altitudinal controls on weathering and erosion. Moreover, they may help explain the altitudinal distribution of excesses and deficits in production of gravel and finer sediment across the catchment (Fig. 3 *A* and *B*). Topography and erosion rates can regulate sediment size by influencing sediment residence times, with slower erosion on gentler slopes leading to longer exposure to weathering (3, 35) and thus finer sediment supplied to channels. This hypothesis is consistent with the observed slower erosion and enhanced delivery of the finer sediment from lower, more gently sloped elevations at Inyo Creek (Fig. 3 *B* and *C*).

Bedrock and Sediment Size. Although the mineralogy and geochemistry of the catchment's three mapped bedrock units are similar enough to fall into the same "granodiorite" category, we cannot rule out the possibility that some of the variations in sediment production are due to altitudinal differences in lithology (Fig. 3*E* and Dataset S2). However, all three units have abundant biotite (ref. 36 and *SI Appendix*), which is widely thought to drive granular disintegration in granitic bedrock (37). Moreover, the highest and lowest units, which dominate the catchment (Fig. 3*E*), are similar in mineral size distribution (*SI Appendix*, Fig. S3) even though the highest unit contains ∼10% K-feldspar megacrysts and the lowest unit contains none (ref. 36 and Dataset S2). The abundant biotite and similarities in mineral size across the catchment may help explain why outcrops of the different bedrock units are similarly prone to rapid granular disintegration on slopes where climate is roughly the same (*SI Appendix*, Fig. S3). Thus, we can be reasonably certain that the deficit in fine sediment production at 3.1–3.5 km (Fig. 3*B*) is not entirely due to an intrinsically lower weathering susceptibility in the highest bedrock unit. Likewise, the fact that the lowest bedrock unit breaks down into a wide range of sediment sizes, both on slopes and in the channel (*SI Appendix*, Fig. S4), indicates that the deficit in gravel production at 2–2.35 km (Fig. 3*A*) is not entirely due to an intrinsically higher weathering susceptibility in underlying bedrock at low elevations. Thus, we deduce that altitudinal differences in lithology are too small to fully explain the differences in erosion and weathering implied by the sediment tracing data. This may not be the case in other, more geologically diverse catchments; rock type can influence both ecosystems (31) and erosion rates (31, 38), and different lithologies can have differences in bedding, jointing, and tectonic deformation in the crust (39). These factors could contribute to intrinsic differences in the sizes of sediment produced on slopes but do not appear to differ enough to drive the observed patterns in sediment production at Inyo Creek.

Climate, Erosion Rates, and Sediment Size. In contrast, differences in climate across the catchment are large and may play a significant role in the altitudinal distribution of excesses and deficits in the production of gravel and finer sediment (Fig. 5). For example, the excess in gravel production from 2.6 km to 2.8 km (Fig. 3*A*) corresponds to a decrease in biomass and an increase in the duration of frost cracking with elevation (Fig. 3 *F* and *G*). Slightly higher up, over the band of deficits in finer sediment from 3.1 km to 3.5 km (Fig. 3*B*), slopes are steep (Fig. 3*D*), erosion is fast (Fig. 3*C*), biomass is negligible (Fig. 3*F*), and the duration of frost cracking is long (Fig. 3*G*). Physical weathering likely dominates over biological and chemical weathering across these elevations, enhancing production of coarse sediment and limiting production of fine sediment (Fig. 5). Meanwhile, both the deficit in gravel (Fig. 3*A*) and excess in fine sediment (Fig. 3*B*) span elevations with relatively gentle slopes (Fig. 3*D*), slow erosion rates (Fig. 3*C*), high biomass (Fig. 3*F*), and negligible frost cracking (Fig. 3*G*); chemical and biological weathering likely dominate over physical weathering processes, thus favoring production of fine sediment and inhibiting survival of coarse particles (Fig. 5), consistent with the observed distributions of apatite helium ages.

Chemical, Biological, and Physical Weathering. The connections shown in Figs. 3–5 are strong, but do not necessarily reflect causation. Nevertheless, they are consistent with the hypothesis that weathering shifts from dominantly biological and chemical near the catchment mouth to dominantly physical in the headwaters, due to altitudinal contrasts in climate and topography. At low elevations, biological and chemical weathering are intense enough, or erosion is slow enough, and soil residence times are commensurately long enough, that coarse rock fragments readily break down to sand and fine gravel before they reach the channel (Fig. 5). Meanwhile, at higher elevations, where physical weathering processes such as frost cracking and rockfall dominate, bedrock shatters into coarser fragments that are delivered rapidly to channels across steep slopes without much additional breakdown (Fig. 5*C*).

Our analysis of just two size classes yields a much richer understanding of sediment supply than one could obtain from either technique alone applied to a single sediment size. Additional data should reveal whether sediment originates from events spanning only the elevations represented by the gravel and finer sediment. If such spatially discrete sediment delivery (e.g., by landsliding) were responsible for the patterns in Fig. 2, it would undermine our analysis of spatial variations in erosion rates (Figs. 3*C* and 4) but not our interpretations of altitudinal variations in sediment size (Figs. 3*A*–*B* and 5).

Apatite ages and cosmogenic nuclides from all size classes in the creek should provide a more comprehensive understanding of how size distributions and erosion rates of sediment vary with elevation across catchment slopes. This should aid in deconvolving the effects of climate, vegetation, erosion, topography, and lithology on sediment production. Optimization algorithms similar to those used here will be vital to inferring altitudinal trends in sediment production that are internally consistent with all of the measured geochemical data. With enough data, it should be possible to account for nonuniform distributions of bedrock apatite (27), deep landsliding (40, 41), wildfires (42), nonmonotonic relationships between age and elevation (25, 43), and other complications not present at Inyo Creek. For example, it will be important to solve for size reduction during transport in catchments where sediment is weak or travel distances are long (6, 44). At Inyo Creek, source bedrock is hard, travel distances are short, and we assume that size reduction during transport is negligible. This assumption is conservative, relative to our conclusions about altitudinal increases in sediment size, because size reduction would be greater for the coarser particles that travel farther from higher elevations.

Our approach integrates over the timescales of sediment production and removal, which is less than 10^4 y due to fast erosion at Inyo Creek. For a longer-term perspective, our approach could be applied to the archive of sediment in the debris fan at the catchment mouth (Fig. 1) to quantify how climate change has influenced sediment production over time. We expect the effects to be significant, based on the strong climatic control on modern sediment production documented here (Fig. 5).

Conclusions

Our study provides a framework for quantifying the climatic and geomorphic controls on the sizes of sediment produced on slopes and delivered to channels. Climate and topography both appear to be important in the trends in sediment size across our study site. The observed altitudinal variations in sediment size and flux

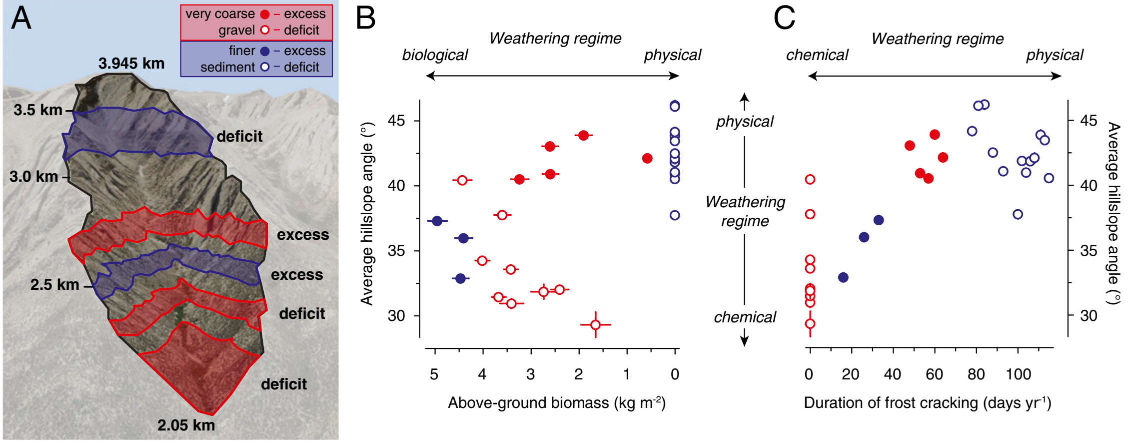

Fig. 5. Climatic and topographic control of the sizes of sediment produced on slopes. (*A*) Oblique view of catchment. Shading marks elevation bands from Fig. 3 of excesses and deficits in production of gravel (red) and finer sediment (blue) relative to the 95% confidence limits on simulated erosion. Plots of hillslope angle against biomass (*B*) and duration of frost cracking (*C*) mark conditions with deficits (open circles) and excesses (filled circles). Excesses in gravel and deficits in finer sediment cluster at elevations where physical weathering may be promoted by steep slopes, low biomass, and long durations of frost cracking. Deficits in gravel and excesses in finer sediment tend to cluster at elevations where chemical and biological weathering may be promoted by gentle slopes, high biomass, and short durations of frost cracking.

are robust, but it is difficult to differentiate climatic, topographic, and lithologic effects without data from more sizes. Hence, we cannot readily predict how sediment production varies with altitude in other catchments that harbor different relationships between altitude, slope, climate, and lithology. However, a more predictive understanding will be obtainable if the approach described here is applied across diverse climatic, lithologic, and tectonic settings. Thus, future applications of the approach will contribute to new process-based understanding of hillslope weathering and erosion in steep landscapes. This, in turn, will permit more mechanistic understanding of grain size variations in channel networks (9, 44) and thus reveal how geology, climate, and topography influence riverine habitats (45). Moreover, as shown here, our approach can improve understanding of the role of sediment supply in the feedbacks between climate, erosion, and tectonics that drive landscape evolution across sites where the origins of sediment can be traced. At Inyo Creek, we found rare empirical support for the hypothesis that the sizes of eroded sediment are coupled to climate and topography through their effects on hillslope erosion, weathering, and sediment production.

Methods

We used standard techniques to isolate quartz and apatite from samples of sand and gravel collected from the active streambed in 2011. To quantify (U–Th)/He ages of apatite, we sent handpicked crystals to California Institute of Technology for analysis of ^{4}He, U, Th, and Sm by noble gas mass spectrometry and inductively coupled plasma mass spectrometry. To quantify ^{10}Be concentrations, we dissolved quartz, spiked it with ^{9}Be, and extracted the Be for analysis of ^{10}Be/^{9}Be ratios by accelerator mass spectrometry at Purdue University.

ACKNOWLEDGMENTS. We thank W. J. Hahm for field assistance, X. Ding for laboratory assistance, and J. W. Kirchner for discussions. Funding was provided by the Ann and Gordon Getty Foundation, an American Geophysical Union Horton Research Grant (to C.E.L.), the Doris and David Dawdy Fund for Hydrologic Research, and National Science Foundation Grants EAR 1239521 and 1325033.

1. Riebe CS, Kirchner JW, Finkel RC (2004) Sharp decrease in long-term chemical weathering rates along an altitudinal transect. *Earth Planet Sci Lett* 218(3-4):421–434.
2. Hales TC, Roering JJ (2005) Climate-controlled variations in scree production, Southern Alps, New Zealand. *Geology* 33(9):701–704.
3. Norton K, von Blanckenburg F (2010) Silicate weathering of soil-mantled slopes in an active Alpine landscape. *Geochim Cosmochim Acta* 74(18):5243–5258.
4. Brantley SL, et al. (2011) Twelve testable hypotheses on the geobiology of weathering. *Geobiology* 9(2):140–165.
5. Marshall JA, Sklar LS (2012) Mining soil databases for landscape-scale patterns in the abundance and size distribution of hillslope rock fragments. *Earth Surf Processes Landforms* 37(3):287–300.
6. Attal M, Lavé J (2006) Changes of bedload characteristics along the Marsyandi River (central Nepal): Implications for understanding hillslope sediment supply, sediment load evolution along fluvial networks, and denudation in active orogenic belts. *Spec Pap Geol Soc Am*, 398, pp 143–171.
7. Sklar LS, Dietrich WE (2001) Sediment and rock strength controls on river incision into bedrock. *Geology* 29(12):1087–1090.
8. Whipple KX (2004) Bedrock rivers and the geomorphology of active orogens. *Annu Rev Earth Planet Sci* 32:151–185.
9. Cowie PA, et al. (2008) New constraints on sediment-flux–dependent river incision: Implications for extracting tectonic signals from river profiles. *Geology* 36(7):535–538.
10. Wobus C, Heimsath A, Whipple K, Hodges K (2005) Active out-of-sequence thrust faulting in the central Nepalese Himalaya. *Nature* 434(7036):1008–1011.
11. Hilley GE, Arrowsmith JR (2008) Geomorphic response to uplift along the Dragon's Back pressure ridge, Carrizo Plain. *Calif Geol* 36(5):367–370.
12. Egholm DL, Knudsen MF, Sandiford M (2013) Lifespan of mountain ranges scaled by feedbacks between landsliding and erosion by rivers. *Nature* 498(7455):475–478.
13. Mudd SM, Yoo K (2010) Reservoir theory for studying the geochemical evolution of soils. *J Geophys Res* 115(F3):F03030.
14. Attal M, et al. (2015) Impact of change in erosion rate and landscape steepness on hillslope and fluvial sediments grain size in the Feather River Basin (Sierra Nevada, California). *Earth Surf Dyn* 3(1):201–222.
15. Whipple KX, Tucker GE (1999) Dynamics of the stream-power river incision model: Implications for height limits of mountain ranges, landscape response timescales, and research needs. *J Geophys Res* 104(B8):17661–17674.
16. Reiners PW, Ehlers TA, Mitchell SG, Montgomery DR (2003) Coupled spatial variations in precipitation and long-term erosion rates across the Washington Cascades. *Nature* 426(6967):645–647.
17. Montgomery DR, Brandon MT (2002) Topographic controls on erosion rates in tectonically active mountain ranges. *Earth Planet Sci Lett* 201(3-4):481–489.
18. Ferrier KL, Huppert KL, Perron JT (2013) Climatic control of bedrock river incision. *Nature* 496(7444):206–209.
19. Willett SD (1999) Orogeny and orography: The effects of erosion on the structure of mountain belts. *J Geophys Res* 104(B12):28957–28981.
20. Montgomery DR, Balco G, Willett SD (2001) Climate, tectonics, and the morphology of the Andes. *Geology* 29(7):579–582.
21. Burbank DW, et al. (2003) Decoupling of erosion and precipitation in the Himalayas. *Nature* 426(6967):652–655.
22. Whipple KX (2009) The influence of climate on the tectonic evolution of mountain belts. *Nat Geosci* 2(2):97–104.
23. Armitage JJ, Duller RA, Whittaker AC, Allen PA (2011) Transformation of tectonic and climatic signals from source to sedimentary archive. *Nat Geosci* 4(4):231–235.
24. Stock GM, Ehlers TA, Farley KA (2006) Where does sediment come from? Quantifying catchment erosion with detrital apatite (U-Th)/He thermochronometry. *Geology* 34(9):725–728.
25. Vermeesch P (2007) Quantitative geomorphology of the White Mountains (California) using detrital apatite fission track thermochronology. *J Geophys Res* 112(F3):F03004.
26. McPhillips D, Brandon MT (2010) Using tracer thermochronology to measure modern relief change in the Sierra Nevada, California. *Earth Planet Sci Lett* 296(3-4):373–383.
27. Tranel LM, Spotila JA, Kowalewski MJ, Waller CM (2011) Spatial variation of erosion in a small, glaciated basin in the Teton Range, Wyoming, based on detrital apatite (U-Th)/He thermochronology. *Basin Res* 23(5):571–590.
28. Granger DE, Riebe CS (2014) *Treatise on Geochemistry*, ed Drever JI (Elsevier, Oxford), 2nd Ed, pp 401–436.
29. Brewer ID, Burbank DW, Hodges K (2003) Modelling detrital cooling-age populations: Insights from two Himalayan catchments. *Basin Res* 15(3):305–320.
30. Ruhl KW, Hodges K (2005) The use of detrital mineral cooling ages to evaluate steady state assumptions in active orogens: An example from the central Nepalese Himalaya. *Tectonics* 24(4):TC4015.
31. Hahm WJ, Riebe CS, Lukens CE, Araki S (2014) Bedrock composition regulates mountain ecosystems and landscape evolution. *Proc Natl Acad Sci USA* 111(9): 3338–3343.
32. Binnie SA, Phillips WM, Summerfield MA, Fifield LK (2007) Tectonic uplift, threshold hillslopes, and denudation rates in a developing mountain range. *Geology* 35(8): 743–746.
33. DiBiase RA, Heimsath AM, Whipple KX (2012) Hillslope response to tectonic forcing in threshold landscapes. *Earth Surf Processes Landforms* 37(8):855–865.
34. Wakabayashi J (2013) Paleochannels, stream incision, erosion, topographic evolution, and alternative explanations of paleoaltimetry, Sierra Nevada, California. *Geosphere* 9(2):1–25.
35. Ferrier KL, Kirchner JW (2008) Effects of physical erosion on chemical denudation rates: A numerical modeling study of soil-mantled hillslopes. *Earth Planet Sci Lett* 272(3-4):591–599.
36. Hirt WH (2007) Petrology of the Mount Whitney Intrusive Suite, eastern Sierra Nevada, California: Implications for the emplacement and differentiation of composite felsic intrusions. *Geol Soc Am Bull* 119(9-10):1185–1200.
37. Wahrhaftig C (1965) Stepped topography of southern Sierra Nevada, California. *Geol Soc Am Bull* 76(10):1165–1189.
38. Hurst MD, Mudd SM, Yoo K, Attal M, Walcott R (2013) Influence of lithology on hillslope morphology and response to tectonic forcing in the northern Sierra Nevada of California. *J Geophys Res* 118(2):832–851.
39. Molnar P, Anderson RS, Anderson SP (2007) Tectonics, fracturing of rock, and erosion. *J Geophys Res* 112(F3):F03014.
40. Niemi NA, Oskin M, Burbank DW, Heimsath AM, Gabet EJ (2005) Effects of bedrock landslides on cosmogenically determined erosion rates. *Earth Planet Sci Lett* 237(3-4): 480–498.
41. Reinhardt LJ, et al. (2007) Interpreting erosion rates from cosmogenic radionuclide concentrations measured in rapidly eroding terrain. *Earth Surf Processes Landforms* 32(3):390–406.
42. Reiners PW, Thomson SN, McPhillips D, Donelick RA, Roering JJ (2007) Wildfire thermochronology and the fate and transport of apatite in hillslope and fluvial environments. *J Geophys Res* 112(F4):F04001.
43. Stockli DF, Dumitru TA, McWilliams MO, Farley KA (2003) Cenozoic tectonic evolution of the White Mountains, California and Nevada. *Geol Soc Am Bull* 115(7):788–816.
44. Sklar LS, Dietrich WE, Foufoula-Georgiou E, Lashermes B, Bellugi DG (2006) Do gravel bed river size distributions record channel network structure? *Water Resour Res* 42(6): W06D18.
45. Riebe CS, Sklar LS, Overstreet BT, Wooster JK (2014) Optimal reproduction in salmon spawning substrates linked to grain size and fish length. *Water Resour Res* 50(2): 898–918.

Supporting Information Appendix

Climate and topography control the size and flux of sediment produced on steep mountain slopes

Clifford S. Riebe [a,1], Leonard S. Sklar [b], Claire E. Lukens [a], and David L. Shuster [c,d]

[a] Department of Geology and Geophysics, University of Wyoming, Laramie, WY 82071, USA
[b] Department of Earth and Climate Sciences, San Francisco State University, San Francisco, CA 94132, USA
[c] Department of Earth and Planetary Science, University of California, Berkeley, CA 94720, USA
[d] Berkeley Geochronology Center, Berkeley, CA 94709, USA
[1] To whom correspondence may be addressed. E-mail: criebe@uwyo.edu

SI Methods

Study Site, Sampling, and Initial Sample Preparation. At our stream-sediment sampling site (36.58886 °N, 118.20289 °W; WGS84), Inyo Creek drains a 3.4 km^2 catchment (Fig. 1, main text). Variations in climate across the catchment's 1887 m of relief are pronounced; mean annual temperature and average annual precipitation range from 10.4 °C and 280 mm at the sampling site to –0.7 °C and 650 mm at the peak, respectively (1). The catchment was not glaciated in the Pleistocene (2). Underlying bedrock throughout the catchment is granodiorite, but it has been mapped as three different units (3). The lowest unit, below ~2600 m elevation, is equigranular, while the highest unit, above ~2600 m is porphyritic (3). The main channel profile lacks the pronounced breaks in slope (i.e., knickpoints) that – if present – might reflect differences in erodibility of underlying bedrock or mark the passage of a wave of incision into the landscape (Fig. S1). We collected a sample of sand (<2 mm diameter) and also 96 individual clasts of very coarse gravel (32–48 mm diameter) from the active creek bed in July 2011. After documenting the general characteristics of each gravel clast (mass, b-axis diameter and rock type; Dataset S3), we crushed them together into mostly monomineralic grains (<1 mm) using a plate pulverizer. The sand was sieved and phi size classes in the 0.25–2 mm range were crushed by size class to 0.25–0.5 mm and recombined according to the original grain size distribution in the sand for analysis of ^{10}Be in quartz.

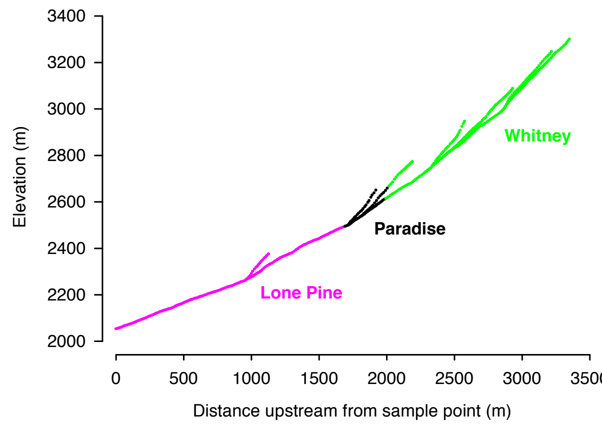

Fig. S1. Channel long profile from 10-m DEM with flow accumulation threshold set at 800 pixels. Colors correspond to mapped extent of three different granodiorite lithologies in the channel bed (3). The lack of pronounced breaks in slope (i.e., knickpoints) suggests there is little along-channel difference in the erodibility of the underlying rock. It is also consistent with a landscape evolution scenario described in the main text.

Apatite-Helium Ages in Detrital Sediment. Apatite was isolated from the pulverized aggregate using gravimetric and magnetic techniques. We then picked individual grains by hand and measured their lengths using a calibrated microscope at the Berkeley Geochronology Center. The dimensions of each grain were used to correct its "raw" apatite-helium age for the fraction of alpha particles retained in each crystal (4). To calculate raw ages, we measured each grain's ^4He concentration using isotope dilution noble gas mass spectrometry (NGMS). Laser-heating techniques used in the ^4He analyses are described elsewhere (5). After measuring ^4He and then dissolving each grain in HNO_3, we measured its U, Th and Sm concentrations using isotope-dilution ICP-MS (Dataset S3). All analyses were conducted at Caltech.

Apatite Analyses. The build-up of ^4He in apatite results from alpha decay of U, Th, and Sm nuclei and their daughter products after the mineral cools during exhumation (i.e., by erosional and tectonic processes) below the ^4He retention temperature threshold, which is typically between 50 and 80 °C, depending on cooling rate and effective uranium concentration (6–8). Hence, measurements of U, Th, Sm, and ^4He in individual apatite grains yield (U-Th)/He ages of sediment particles that carry the apatite. Calculated ages of apatite separated from the gravel are reported in Dataset S4, along with analytical uncertainties in individual measurements of U, Th, and ^4He. Ages range from 28.1 to 67.5 Myr. One standard error was an average of ±2.8% of the measured value (range = 2.1–3.3%).

Inferring Erosional Source Elevations from Individual Crystal Ages. Detrital thermochronometric ages are commonly used in studies of the timescales of tectonic exhumation (9–11), but here they serve as tracers of the source elevations of gravel and finer sediment in the creek (12–14). Inferring source elevation from ages is possible at Inyo Creek because apatite-helium ages in bedrock increase systematically with elevation (Fig. 1, main text). The age-elevation relationship (Fig. 1) is based on nine bedrock ages from previous studies of Inyo Creek (12) and the vicinity (15). For completeness, and because we must report two minor revisions to the elevations given in one of the original reports (15), we reproduce the bedrock ages and their corresponding elevations in Dataset S1.

The age-elevation data define an inverse-variance-weighted, least-squares regression of the form

$$t = c + d\left(Z - Z^{*}\right) \tag{S1}$$

Here, t is the apatite-helium age, Z is elevation in kilometers, Z^{*} is a reference elevation, here equal to 2.962 km (the mean of the elevations in Dataset S1), c is 44.2±1.8 Myr, the age evaluated at Z^{*}, and d is the best-fit regression slope, equal to 23.7±2.8 Myr km^{-1}. The coefficient of determination (r^2) is 0.90 ($p<0.0001$). Equation S1 permits conversion of ages to elevations; t is generally known from the measurements of U, Th, Sm and He, such that we can solve for Z, the inferred erosional source elevation of the apatite crystal. The inferred elevations are reported in the last column of Dataset S4.

Cumulative Age Distributions and Synoptic Frequency Distributions. With our suite of measured ages, we constructed cumulative age distributions (CAD's) following simple procedures outlined in ref. (13). We also constructed a CAD for bedrock ages in the catchment by filtering the elevation distribution – extracted from a 10-m resolution Digital Elevation Model (DEM) – through Eq. S1. We then used these CADs in Kolmogorov-Smirnov (K-S) and Kuiper tests for differences in the age distributions, as described later.

In our analysis of differences in the source elevations of the different sizes of sediment, it is not enough to know whether or not the distributions are different, which is what standard K-S and Kuiper tests reveal. Rather, we also needed to know where (i.e., over which elevation ranges) the distributions are different, so that we can identify source elevations with low and high relative rates of sediment production and delivery. To do so, we first generated synoptic age distribution functions (9, 13), $f(t)$, similar to a probability distribution function of ages, by evaluating Eq. S2 for all measured ages at each plotting position (t) in the function.

$$f\left(t\right) = \frac{1}{n}\sum_{i=1}^{n}\left(\sqrt{2\pi}\sigma_i e^{\left(t-t_i\right)^2/2\sigma_i^2}\right)^{-1} \tag{S2}$$

Here n is the number of measured ages, in this case 73 for the gravel, and 52 for the finer sediment. The uncertainty in each age (σ_i) is the propagated analytical uncertainty from the isotopic analyses (13). Since ref. (12) does not report analytical uncertainties in ages of the finer sediment, we used the average percentage analytical uncertainty from the very coarse gravel measured in our analysis (from Dataset S4) as an estimate of the percentage analytical uncertainty on each of the previously measured 52 ages of finer sediment. This should be reasonable given the tight distribution in percentage errors (mean and standard deviation: 2.76±0.27%). For completeness, we include Dataset S5, which lists the ages of the finer sediment, along with the reported uncertainties from ref. (12), our estimates of the analytical errors, and the inferred source elevations of the ages based on Eq. S1. In Eq. S2 the analytical uncertainties are incorporated into the synoptic age distribution directly in the way the equation spreads each discrete age (t_i) into a normal distribution. The result is a normalized frequency distribution of ages from each size class. Results for both the gravel and finer sediment are shown in Fig. S2.

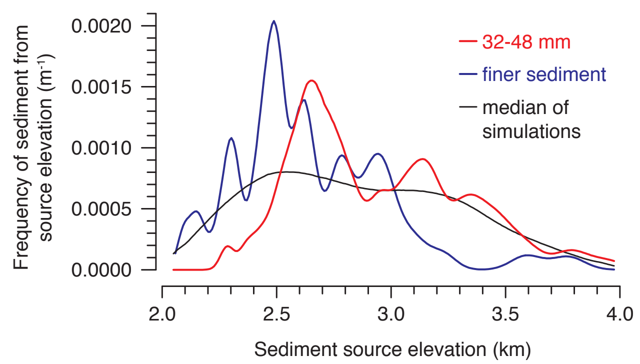

Fig. S2. Frequency distribution of sediment source elevations for gravel (red) and finer sediment (blue) inferred from Eq. S2 using elevations from Datasets S4 and S5. Black line shows median of 30,000 simulations of "uniform" erosion (described in text).

Statistical Tests for Differences in Ages. The variances in the ages of very coarse gravel and finer sediment yield a variance ratio that is less than the corresponding critical value for the F distribution ($p = 0.245$) in a variance-ratio test. This prompted us to calculate a pooled variance of 85.5 Myr^2 for our t test of the significance of the difference between the mean ages. We found that the difference is highly significant ($p = 0.0004$). However, because the distributions are skewed, we also performed a nonparametric Mann Whitney rank sum test on the distributions. It suggests that the difference is significant at a level of p = 0.0003. We then used Hodges Lehman estimators to calculate the median and 95% confidence interval of paired differences between the ages, as a robust estimate of the magnitude of the difference in ages. Our analysis yields the following values: 6.3 (3.5–9.6) Myr for the median and its 95% confidence interval on the paired differences in age; and 266 (149–404) m for the median (and its 95% confidence interval) of the corresponding paired differences in elevation.

We also tested for differences in the cumulative age distributions (CADs). Kuiper's test (16, 17) has been a common choice in recent work (9, 12), in place of the more widely known Kolmogorov-Smirnov (K-S) test. We performed both types of tests here using standard methods. Because the Kuiper test is less widely known, and because we obtain a different result than ref. (12) for the difference between the finer sediment and the bedrock (Dataset S6), we explain the procedure we used in the text that follows. Following ref. (17), we calculate the Kuiper's probability (Q_{KP}) of a measured offset of one CAD relative to the other under the null hypothesis that they are the same.

$$Q_{KP}(\lambda) = 2\sum_{j=1}^{\infty}\left(4j^2\lambda^2 - 1\right)e^{-2j^2\lambda^2} \tag{S3}$$

The sum in Eq. S3 represents an asymptotically convergent series and λ is calculated according to Eq. S4.

$$\lambda = V\left(\sqrt{N_e} + 0.155 + {0.24}/{\sqrt{N_e}}\right) \tag{S4}$$

Here, N_e is the effective number of samples, equal to $N_1N_2/(N_1+N_2)$, where N_1 and N_2 are the smaller and larger numbers of samples in the two distributions, respectively. V is the Kuiper statistic, calculated from Eq. S5.

$$\begin{aligned} V &= D_+ + D_- \\ &= \max_{-\infty<t<\infty}\left(CAD_2(t) - CAD_1(t)\right) \\ &\quad + \max_{-\infty<t<\infty}\left(CAD_1(t) - CAD_2(t)\right) \end{aligned} \tag{S5}$$

Here, D_+ is the maximum difference between the younger and older CADs (denoted by CAD_2 and CAD_1, respectively) and D_- is the maximum difference between the older and younger CADs. Results of the Kuiper tests are reported in Dataset S6, along with results of the more standard K-S test.

All of the Kuiper and K-S comparisons of the data sets reveal significant differences in the CADs. Yet these tests do not reveal the elevation ranges over which the distributions differ and thus are not able to pinpoint connections between differences in sediment production and variations in climate and topography across catchment slopes. In particular, we are interested in identifying the elevation ranges over which the age distributions in our samples differ in a statistically detectable way from the age distribution in the bedrock. To quantify the elevation ranges over which the measured ages depart from what we would expect based on a random sampling of catchment bedrock, we applied a bootstrapping approach to estimate the range of plausible outcomes of age distributions for each sediment sample (i.e., for 73 ages in the case of the gravel and 52 ages in the case of the finer sediment). Here we adopt the null hypothesis that each point on the landscape has an equal probability of contributing a grain of sediment to the creek in any interval of time. To simulate this process, we used the following procedure: 1) identify a source elevation for a clast sampled from the creek by randomly sampling the bedrock elevation distribution; 2) calculate the age and an associated standard error of the apatite grains in the clast using Eq. S1; 3) assign an age to the measured apatite grain by randomly sampling a normal distribution with a mean and standard deviation equal to the calculated age and standard error from step 2; 4) repeat steps 1–3 *n* times, where *n* is the number of ages measured in the sample collected from the creek; 5) assign an estimated analytical error of each of the *n* ages from steps 1–4 by randomly sampling (with replacement) the distribution of analytical errors in the ages of the gravel (Dataset S4); and 6) use the distribution of randomly sampled ages (steps 1–4) and their randomly sampled analytical errors (step 5) in Eq. S2 to construct a synoptic age distribution function.

By repeating steps 1–6 many times (in this case, 30,000) for the gravel (n = 73 in step 4) and the finer sediment (n = 52 in step 4), we simulated the range of possible outcomes of measured age distributions for the case of uniform erosion. We then determined the percentiles associated with the distribution of outcomes at each elevation. The 2.5th, 10th, 25th, 75th, 90th, and 97.5th percentiles are plotted with labeled gray lines in Figs. 3*A–B* in the main text. We then compared the simulations with the synoptic age distribution functions of measured ages at each elevation to identify the elevation ranges over which the production and erosion of gravel and finer sediment differ from the null hypothesis. To focus on differences in the measured distributions relative to the null hypothesis, we normalize them to the median of simulations at each elevation in Fig. 3.

Cosmogenic Nuclides, Erosion Rates and Sediment Mixing. Cosmogenic nuclides build up in minerals near Earth's surface due to interactions with cosmic radiation, which has a known flux and capacity to create cosmogenic nuclides like ^{10}Be in minerals such as quartz. Hence the concentrations of these nuclides in rock and sediment reflect near-surface residence times; if erosion to the surface is slow, minerals will have long residence times and thus long exposure to cosmic radiation, and vice versa. Thus measurements of cosmogenic nuclide concentrations (N) in soils and sediment can be used to infer erosion rates (E) in landscapes (18), as indicated in Eq. S6.

$$\langle N \rangle = \frac{\langle P \rangle \Lambda}{\langle E\rho \rangle} \qquad \text{(S6)}$$

Here, the brackets denote areal averages, P is the production rate of cosmogenic nuclides at the surface, ρ is density of the rock or soil, and Λ is an exponential scaling factor for nuclide production (equal to ~160 g cm^{-2} for cosmogenic ^{10}Be), which accounts for the attenuation of cosmic radiation (and its ability to produce cosmogenic nuclides) with depth in matter for Earth materials. Additional terms are needed to account for production due to cosmogenic muons (19). Equation S6 implies that the spatially averaged erosion rate for a contributing area can be inferred from cosmogenic nuclide concentrations measured in stream sediment. One proviso is that erosion rates are fast enough that radioactive decay can be ignored (20). This should generally be true for ^{10}Be, which has a half life of 1.39 Myr (21, 22). The approach outlined in Eq. S6 has been widely used to quantify how erosion rates vary from one catchment to the next across landscapes. In our forward modeling exercise (the basis of results presented in Fig. 3*C*), we use the principles underpinning this formulation and assume that each point on the landscape delivers sediment to the stream in proportion to its erosion rate.

Cosmogenic ^{10}Be Measurements. Using standard magnetic and froth-floatation techniques, we isolated quartz from the pulverized aggregates of gravel and sand. The quartz was then chemically purified (23, 24), spiked with a high-purity Be carrier, with ^{10}Be/^{9}Be ratio ~1×10^{-15} (25), and dissolved in HF and HNO_3. We extracted Be from the dissolved quartz following standard procedures at the University of Wyoming. Once the samples were prepared and packed into targets, their ^{10}Be/^{9}Be ratio was measured by accelerator mass spectrometry (AMS) at the Purdue Rare Isotope Measurement (PRIME) Lab (26). The ^{10}Be/^{9}Be ratio in the process blank paired with these samples was 6(±2)×10^{-15}. We calculate ^{10}Be concentrations of 1.01(±0.05)×10^{5} atoms g^{-1} for quartz from the gravel and 1.82(±0.06)×10^{5} atoms g^{-1} for quartz from the sand (Dataset S7). The result from the gravel was used together with the ^{10}Be concentration from the finer sediment from the previous Inyo Creek study (12) in our optimization analysis of spatial variations in erosion rates. We note, however, that the ^{10}Be in the finer sediment from the previous work was measured at PRIME Lab on 23 July 2005 (PLID 200501488), prior to now routine use of ICN standards that are calibrated (27) to the revised ^{10}Be half life (21, 22). Thus we had to correct the ^{10}Be concentration from the previous study by a factor of 0.9, from 1.73(±0.01)×10^{5} (reported in ref. (12)) to 1.557(±0.009)×10^{5} atoms g^{-1}, for consistency with the more accurate standardization of the ^{10}Be in the gravel (24).

Optimization Analysis. Our optimization analysis employs a forward model of ^{10}Be concentrations in quartz from the gravel and finer sediment and an imposed altitudinal gradient in erosion rates. Each point in the landscape has an elevation (from the DEM) and thus an apatite-helium age determined from the age-elevation relationship (12) (Fig. 1). Each point also has a cosmogenic nuclide concentration set by both the local erosion rate (which is imposed and modulated in the optimization algorithm) and the local ^{10}Be production rate (18). We explicitly account for ^{10}Be production by muons (19, 28) and use a standard scaling scheme (29–31) to adjust the assumed sea-level, high-latitude spallogenic production rate of 4.5 atoms g^{-1} yr^{-1} (31) to each point in the catchment. Cosmic ray shielding by snow (32) and topography (33) are accounted for using local snow-course data (34) and the DEM, respectively (see notes in Dataset S7 for details).

In our model, we assume that sediment eroded from each point is represented in proportion to its erosion rate and area (where area is the size of a pixel) in the mixture of stream sediment at our sampling point (Eq. S6). This is consistent with conventions used in previous cosmogenic nuclide studies (20, 35, 36). However, our model is distinct from previous work in its separate treatment of sediment of different sizes. Thus it can readily account for the measured altitudinal variations in sediment delivery among the different sizes (Fig. 2).

Frost Cracking Duration and Other Explanatory Variables. To estimate the time spent in the frost-cracking window at each elevation (Fig. 3*F*), we first estimated the mean annual temperature at each elevation using the PRISM database (1). We then converted the temperatures into the number of days with temperatures between –3 and –8 °C at each elevation using a sinusoidal daily temperature variation with amplitude = 11 °C and period = 365 days. This should yield a realistic estimate of the fraction of time spent in the frost-cracking window by the landscape surface at each elevation in an average year.

Dataset S8 also includes values of the age distributions (normalized by subtraction to the mean of the 30,000 simulations), the fractional coverage by each of the catchment's three mapped lithologies, and spatially averaged values of hillslope angle and above-ground biomass. All data are reported in Dataset S8 with corresponding elevations. Each value in the dataset is either integrated or averaged over successive 30 m elevation windows (see table notes for details).

Bulk Geochemistry and Grain Sizes of Minerals. To supplement existing data on bedrock geochemistry from ref. (37), we collected bedrock from 16 widely distributed locations for bulk geochemical analysis of the three lithologies mapped in the catchment. A sledgehammer or gas-powered drill was used to obtain fresh samples. In the lab, we ground subsamples of this material to <50 m in a tungsten carbide grinding pot using a SPEX shatterbox. After driving off water and any volatiles in a muffle furnace at 550°C for 12 hours, we generated fused beads of carefully massed powder and lithium tetraborate (typically at a ratio of 1:9) and measured concentrations of major elements in the samples by x-ray fluorescence at the University of Wyoming. Results are reported in Dataset S2

At two sites, we also sampled slightly weathered (i.e., partly disaggregated) rock from outcrops, exploiting natural granular disintegration in the field to aid in breaking minerals apart in the lab for determination of mineral size distributions. One sample came from Lone Pine Granodiorite and the other came from Whitney Granodiorite. We measured the size distributions of the minerals in each sample by sieving after disaggregating the grains by hand and with a rubber mallet under gentle pressure. The results are reported in Fig. S3.

SI Discussion

Anomalous Ages. A total of 80 ages were measured in apatite crystals plucked from the crushed sample of very coarse gravel. However, there are seven estimates that fall outside the plausible range of ages, which we calculate to be 22.5–67.5 Myr, based on the age-elevation relationship (Eq. S1) and the 2045–3947 m elevation range in the catchment. Six of these aberrant ages (i.e., grains 6, 7, 10, 29, 30, and 72; Dataset S4) are older than the measured crystallization ages in the bedrock (~85 Myr) (3). Hence, we can exclude them from our analysis because apatite-helium ages cannot plausibly be older than the rock itself. Nevertheless, this raises the question of why their apparent ages are so high. Although the apatite crystals were carefully screened for visible mineral inclusions, there is a chance that micro-inclusions of zircon (i.e., with high U and Th content relative to the host apatite) exist in some or all of the grains. Zircon is insoluble in the presence of nitric acid; hence any zircon inclusions in our grains, if present, would not have dissolved during sample preparation. In that case, the

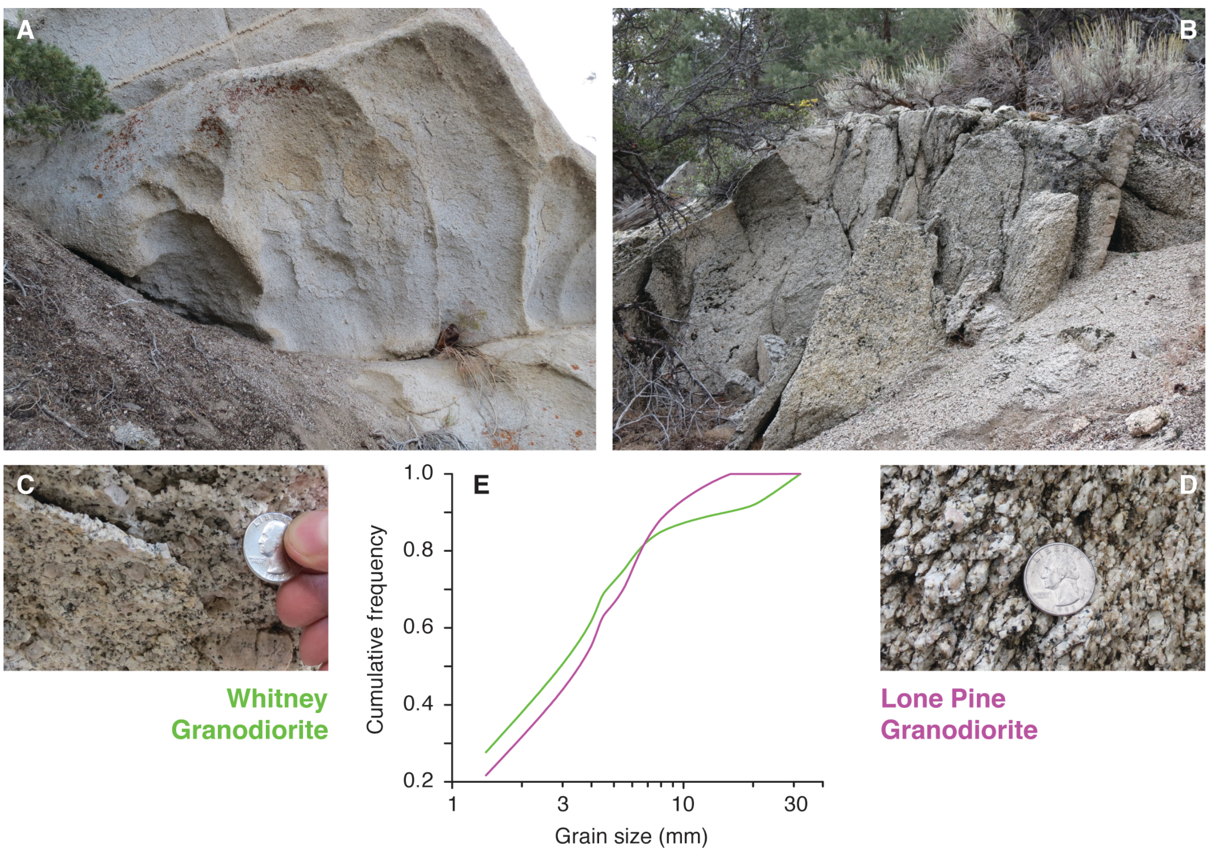

Fig. S3. Granular weathering and grain size. Outcrops of both the Whitney (*A*) and Lone Pine (*B*) granodiorites often exhibit extensive granular disintegration. Example in (*A*) is from the nearby Lubkin Creek catchment, where Whitney Granodiorite crops out at the same elevations (in this case at 2,290 m) as Lone Pine Granodiorite on Inyo Creek slopes. The evidently similar ease with which the two rock types break down by granular disintegration (*C-D*) at similar elevations suggests that differences in bulk geochemistry and mineralogy probably play minor roles in the differences in sediment production shown in Fig. 2 in the main article. Although the Whitney contains up to 10% large potassium feldspar phenocrysts, the grain size distributions of minerals are very similar overall between the two lithologies (*E*).

daughter product (^4He) would have been measured by NGMS, while the parent nuclides (of U and Th) associated with insoluble zircon would not have been detected by ICP-MS, leading to anomalously old apparent apatite-helium ages. We suggest that the older-than-plausible ages (highlighted in Dataset S4 with italics and asterisks) probably reflect unmeasured parent nuclides in insoluble zircon micro-inclusions.

The aberrantly young (10.3 Myr) age of crystal 14 is more enigmatic. It could, for example, reflect partial resetting of ^4He due to wildfire-induced heating (38). However we suspect this phenomenon is uncommon at Inyo Creek, due to the lack of vegetation (Fig. 3*E*); with limited fuel for wildfires, it seems unlikely that the catchment could support the long, intense fires needed to reset ^4He in apatite (38). Similar arguments were made about ages from detrital apatite in the finer sediment (12). Furthermore, it has been noted (12) that paleoecological evidence from nearby Owens Lake suggests that forests in the Sierra Nevada were less extensive during glacial times (39). This implies that fuel for wildfires at Inyo Creek was even less abundant in the past than it is today.

In addition to simply being too young, crystal 14 also has U and Th concentrations that are extremely high relative to any other crystal analyzed here. This gives us a statistical basis for excluding it and moreover points to possible analytical problems in the U and Th analyses as an alternative to the wildfire explanation for the low inferred age. In any case, we exclude it from the analysis along with the six ages that exceed the crystallization age of the Inyo Creek catchment bedrock. Hence, in calculating the distributions reported in Fig. 2, we used 73 of the 80 measured ages for gravel. Including the excluded ages would not substantially change the results of our comparisons; the average age would be somewhat different (i.e., 46.5 Myr with the aberrant ages included compared to 44 Myr without), as would the median (i.e., 43.9 Myr with compared to 41.6 Myr without), though not by enough to substantially alter our results. In fact, we would actually conclude that gravel originates from even higher elevations on average than we do without the outliers. Including them would therefore amplify (not eliminate) one of the major results reported in the main article.

Our exclusion of ages that fall outside the plausible range for the catchment ultimately raises questions about the reliability of ages that fall within the range as well. For example, it is possible that grains with ages that fall within the limits defined by catchment bedrock also contain undetected zircons, and thus higher-than-measured parent nuclide concentrations. However, our analysis is robust against this type of bias to the extent that the gravel, finer sediment, and bedrock age distributions are all similarly prone to it; in our evaluation of the null model of uniform erosion, the apatite-helium ages in gravel and finer sediment are compared to the bedrock age distribution, which is ultimately based on ages of apatite from the same bedrock substrate that produced the sediment. Thus, the bedrock samples should exhibit the same bias as the samples of gravel and finer sediment, to the extent the bedrock age distribution is based on apatite grains that also contain a share of undetected zircons. As a result, we cannot rule out the possibility that the absolute ages measured here are biased somewhat by undetected zircons. However our use of these ages as tracers of source elevations is not biased, provided that apatite crystals sampled for the age-elevation relationship (Eq. S1) are representative of apatite crystals sampled for the detrital analyses.

Differences in Age Distributions. Inputs and outputs of our paired tests of CADs are reported in Dataset S6. We calculated Kuiper's V from CADs as described above. Values of Q_{KP} represent probabilities of the largest differences in distributions (i.e., V) under the null hypothesis that the CADs are the same. Hence, a value of 0.05 for Q_{KP} indicates that a difference of V or bigger would arise by chance 5% of the time when the distributions are in fact the same. The comparisons of finer sediment versus bedrock and finer sediment versus gravel yield p values of 0.007 and 0.002 respectively (Dataset S6). Meanwhile, the Kuiper test of the CAD of gravel versus the CAD of bedrock yields a p value of 0.02.

In our Kuiper test of the age distributions of bedrock and the finer sediment, the assessment of significance differs markedly from results reported in the study that originally published the ages of the finer sediment (cf. ref. (12)). In that study, the two distributions were judged to be not significantly different (12), based on Kuiper testing, whereas here, we judge them to be different with a significance level of $p = 0.007$ (Dataset S6). The difference likely arises from differences in the way the Kuiper test was employed. Here, we employed the Kuiper test in the standard way, as outlined in Kuiper's original paper (16) and as summarized in modern statistical texts (17); the cumulative distributions (our CADs, constructed following procedures in ref. (13)) of each pair of measured populations were compared in a single test (in this case, between the ages in finer sediment and the ages in bedrock).

Differences in Nuclide Concentrations. The calculation of spatially averaged erosion rates from cosmogenic nuclides assumes that $\langle P \rangle$, the spatially averaged production rate of ^{10}Be, can be reliably estimated (Eq. S6). To estimate $\langle P \rangle$, studies often use standard scaling methods (31) to evaluate the production rate at each elevation in the catchment and then take the average of the production rates thus inferred. However, at Inyo Creek, the distribution of source elevations and thus the average $\langle P \rangle$ is different for each size class. This shows that the assumption that $\langle P \rangle$ can be reliably calculated from the elevation distribution is not always valid. At Inyo Creek, because the coarser sediment originates from higher elevations on average, it also experiences a higher $\langle P \rangle$ than the finer sediment. This implies that nuclide concentrations would vary with particle size even if erosion rates were uniform across a catchment, because of variations in $\langle P \rangle$ among the particle sizes.

Alternative production rate biases have been invoked to explain differences in nuclide concentrations across samples with different sediment sizes (36, 40, 41). For example, in sediment from Puerto Rico catchments (36), such variations in nuclide concentrations have been attributed to effects of landsliding, under the assumption that landslides generate coarse sediment with low nuclide concentrations by liberating it from depths shielded from cosmic radiation. In contrast, in the Smokey Mountains catchments (40), where landsliding does not appear to be very frequent on slopes, observed decreases in nuclide concentrations with increasing particle size may reflect a lower erosional source elevation and thus a lower average production rate for the coarse sediment (40). This could arise if the breakdown of particles in the stream eliminates coarse sediment eroded from high elevations in the catchment headwaters, such that coarse sediment in the stream at the sampling point is derived from mostly lower elevations. In that case, differences in nuclide concentration might reflect effects of comminution in streams (40), rather than differences in the particle sizes of sediment produced on slopes. At Inyo Creek, the apatite-helium ages show that gravel clearly originates from higher, not lower elevations (Fig. 2). Moreover, breakdown rates are likely low at Inyo Creek, due to the short travel distances and hard, granodiorite source material.

An additional bias can arise when the target mineral for nuclide production (usually quartz) varies in concentration with elevation in the underlying bedrock. If it does, the production rate would either be overestimated or underestimated depending on whether quartz content decreases or increases with elevation. We have no basis for expecting variations in quartz concentrations at Inyo Creek; all of the underlying bedrock is granodiorite (3) with quartz concentrations ranging from 20 to 30% by volume (37).

In our study, we can quantify the difference between the cosmogenic nuclide production rates of the two size classes, because we know (from the apatite-helium data) the source elevations of the gravel and finer sediment. We estimate that the gravel originates from ~300 m higher on average (Dataset S7) and thus has a 19% higher average nuclide production rate (31). This would impart the gravel with a higher ^{10}Be concentration, relative to the finer sediment, if the overall erosion rate (for all size classes combined) were spatially uniform in the catchment. Instead we find that the gravel has a markedly lower nuclide concentration relative to the finer sediment. This implies that erosion rates are not spatially uniform but instead increase with elevation across catchment slopes; an altitudinal increase in erosion rates can explain the lower ^{10}Be in the gravel, despite its higher average source elevation and correspondingly higher ^{10}Be production rate.

An alternative explanation for the discrepancy in nuclide concentrations is that gravel is eroded from depths that are shielded from cosmic radiation, while the finer sediment is derived from the surface. To evaluate this possibility, we estimated that the shielding depth for gravel would need to be 45 cm across the entire catchment to produce the observed nuclide concentrations for the limiting case that finer sediment is derived solely from the surface and gravel is derived solely from depth. This is a minimum estimate of the depth of landsliding that would be needed across the entire catchment to explain the difference in nuclide concentrations. In the more likely event that at least some of the finer sediment is derived from depth and some of the gravel is derived from the surface, the catchment-wide depth of landsliding would need to be significantly greater. We consider this scenario to be unlikely.

Difference in Sample Location. In picking our sampling point, our intent was to sample as closely as possible to the sampling point of the finer sediment in ref. (12). Using the available information in ref (12), we chose a site spanning ~30 m of channel length at an elevation along the creek of 2060 m (36.58886°N, 118.20289°W; WGS84). Here, the total catchment relief is 1887 m (measured to the summit of Lone Pine Peak), closely matching the reported relief at the sampling point of the finer sediment (i.e., 1905 m – see page 726 in ref. (12)). However, we have subsequently learned that the sampling site of the finer sediment in 2002 was located at 36.591983°N, 118.199661°W, at an elevation of 1950 m (corresponding to 1997 m of total relief).

The difference in sampling locations in 2002 and 2011 raises the question of whether it might significantly confound the inferences and interpretations in our analysis of sediment production and erosion. There are several reasons why we can be reasonably certain that this is not the case. First, our interpretations relate to spatial variations in sediment production and erosion across an entire catchment, and the differences in catchment area for the two sampling points is only 0.1 km^2, or about 3% of the 3.4-km^2 catchment area at our 2011 sampling point. This is too small to lead to a significant difference in the distribution of apatite-helium ages. In fact, only one of the analyzed apatite grains, 02TEIC01-045, has an age that implies a source elevation that falls within the extra sliver of area encompassed by the slightly larger 2002 study catchment (Dataset S5). The implied source elevation of that grain is 2090 m. Only ~20% of the length of the 2090 m contour line in the larger catchment is unique to the larger catchment, implying that there is an 80% chance that the lone, potentially confounding apatite grain actually originated on a slope that falls within both catchments (and thus is not confounding at all). Hence, our comparison of apatite-helium age distributions is insensitive to the difference in sample location.

The analysis of ^{10}Be in detrital quartz is more prone to confounding effects of differences in sample location because it integrates over thousands of sediment grains – i.e., many more than the 125 analyses of detrital apatite-helium ages. Hence it is likely that the sample of quartz from the previous study had at least a few grains that originated from the extra sliver of area unique to the larger catchment. Even so, these grains almost certainly made up a small fraction of the total number of grains sampled, and thus were not abundant enough to strongly influence the results. This is corroborated by ^{10}Be in quartz from our sample of sand collected in July 2011 at the 2060 m elevation site. Our sand, with grain sizes ranging from 0.25 to 2 mm, was finer than the ref. (12) sample, which consisted of 60% coarse sand, plus 30% pebbles and 10% coarser sizes up to 40 mm. (To dispel any semantic confusion about which sample is which, we remind the reader that we call the ref. (12) sample the "finer sediment" elsewhere in the SI and the main text because of its relationship to the 32–48 mm particles that we focused on in our study.) Given that gravel originates from higher elevations, which we inter to be eroding faster than lower slopes, where finer sediment originates (Figs. 2 and 3*C*), we would expect a sample consisting of just sand to have a higher cosmogenic nuclide concentration (due to the slow erosion rates at low elevations) than a mix of sand, pebbles, and gravel, such as the one analyzed in ref. (12). This expectation is consistent with our observations (see Dataset S7): the ^{10}Be concentration in the sand collected in 2011 is $1.82(\pm0.06)\times10^5$ atoms g^{-1}, compared with the corrected value of $1.56(\pm0.01)\times10^5$ atoms g^{-1} in the mixture of sand, pebbles, and gravel collected in 2002 (12). This internal consistency in ^{10}Be concentrations suggests that there is good agreement in ^{10}Be concentrations from one place to the next over short distances in the creek. It also suggests that there is good year-to-year consistency in sediment sourcing from catchment slopes, implying that the results reported in Figs. 2–5 in the main text provide a robust picture of sediment production and erosion from the catchment. Together, our considerations of plausible effects of sediment inputs from the extra sliver of area in the larger catchment indicate that the difference in sampling locations is not a significant confounding factor in our analysis.

Differences in Lithology. Bedrock throughout the catchment is granodiorite, consisting of three mapped units (3): the Lone Pine Granodiorite (Klp), in the lower 30% of the catchment; the Paradise Granodiorite (Kp), in a narrow band of area at mid elevations; and the Whitney Granodiorite (Kw), in the upper 60% of the catchment (Fig. 3*G*, main text). The Klp unit, which intruded the Sierra Nevada Batholith during the early stages of the Whitney Intrusive Series, differs somewhat from the Kw and Kp units in both texture and composition (37). Klp is roughly equigranular, whereas Kw and Kp are both porphyritic, with potassium-feldspar phenocrysts. Meanwhile, Klp has about 10% less silica, more calcium and iron, and ~6% hornblende, compared to 2.5% or less of this mafic mineral in Kp and Kw (Dataset S2).

The altitudinal differences in lithology raise the possibility that they significantly confound our analysis of climatic and topographic effects on sediment production and erosion (Figs. 3–5). However, there are several reasons why we can be reasonably certain that this is not the case. We elaborate on relevant observations from the field and a review of the literature in the paragraphs that follow.

All three units contain biotite (37), a mineral that has been widely implicated in the production of "grus" – i.e., the granular disintegration of granitic bedrock into mineral-sized grains (42–46). (Here "granitic" generically refers to rock types encompassing granodiorite, tonalite, quartz diorite, granite and other similar plutonic rocks.) Biotite can grusify bedrock by cracking it along mineral-grain boundaries due to stresses produced as individual biotite grains expand during reactions with water (42). Biotite is somewhat more abundant in Klp than Kp and Kw, with an average of 7.1% by volume versus 5.5 and 4.3% by volume, respectively, based on samples collected in previous work from outcrops near the Inyo Creek study catchment (see Dataset S2, ref. 37). This raises the possibility that altitudinal differences in biotite content drive the measured differences in sediment production. However, observations from catchment slopes suggest that any effects of differences in biotite content are small compared to the effects of altitudinal differences in climate and topography. For example, outcrops of the different granodiorite lithologies exhibit no obvious differences in propensity to break down into mineral-sized particles via granular disintegration: Kw and Klp (the most different pairing of the three units) both exhibit extensive granular disintegration in outcrops across the catchment and elsewhere in the region. A specific example is shown in Fig. S3: In the Lubkin Creek catchment, which is just 12 km south of Inyo Creek, Whitney Granodiorite underlies the same elevations as Lone Pine Granodiorite on Inyo Creek slopes, offering an opportunity to search for differences in granular disintegration without the confounding effects of differences in climate (Fig. S3). Both units seem able to readily grusify in outcrops at similar elevations (Figs. S3*C–D*). Thus we infer that differences in bulk geochemistry and mineralogy play minor roles in the differences in sediment production shown in Fig. 2 in the main article. In particular, the deficit in finer sediment production at high elevations (Fig. 3) cannot be explained by an intrinsic inability of Kw to grusify into small fragments. Instead, the deficit appears to be due to the steeper slopes, colder temperatures, and lower above-ground biomass that are characteristic of higher elevations in the catchment (Fig. 5).

The lack of a strong connection between biotite content and grussification, based on physical evidence we have gathered from Inyo Creek and surrounding catchments (Fig. S3), is broadly corroborated by the literature on biotite weathering in granitic bedrock. For example, in a study of landscape evolution on the west side of the Sierra Nevada, the presence of biotite in any amount was found to be sufficient to drive the development of the "stepped" topography that characterizes the region (42); differences in the breakdown of granite, which evidently result in the juxtaposition of steeply sloped "steps" and gently sloped "treads", are caused by differences in exposure to water of bare rock relative to bedrock mantled by soil (42). On bare bedrock, water from precipitation runs off before it can react with biotite. Meanwhile, bedrock mantled in soil is more readily decomposed, because the water seeps into the subsurface and reacts with biotite in the bedrock. Thus, at other Sierra Nevada sites where granite weathering has been studied, differences in exposure of bare rock, not biotite abundance, appear to drive significant differences in weathering at the landscape scale.

Additional insight on the role of biotite in grussification can be gained from a study of weathering in the Laramie Range, Wyoming, USA, which exhibits bimodal topography, with bare bedrock tors cropping out of a low-relief erosion surface (43). The granitic bedrock that comprises the high-standing tors has 8.1% biotite compared to just 2% biotite in granitic bedrock under the more deeply weathered erosion surface. Thus, biotite is four times more abundant in the tors, which seem more resistant to weathering than the low-relief erosion surface. This is opposite to the effect needed to preferentially produce coarser sediment from a more biotite-poor bedrock, and thus confound our analysis of climatic and topographic effects on sediment production at Inyo Creek. In the Laramie Range study, the deep weathering of the low-relief surface was attributed to Precambrian hydrothermal alteration of biotite (not biotite abundance), which evidently affected the bedrock under the low-relief surface, but not the bedrock that comprises the tors (43). Thus, a connection between biotite abundance (when it is present) and resistance to weathering is not supported by landscape-scale studies of weathering in either the Sierra Nevada (42) or the Laramie Range (43).

Studies of weathering at smaller scales have been more ambiguous. In one road cut in Colorado, USA, grussified bedrock has more biotite than a sub-vertical slab of fresh bedrock and the relatively coherent corestones that have been exposed by the cut (44). However, the scale of the cut is very small, spanning just 100 m. Hence, the broader significance of the observations is unclear. Moreover, the biotite content reported for the grus is potentially misleading because it was not corrected for weathering losses implied by immobile element enrichment (47).

Elsewhere, in British Columbia, Canada, a study of differential weathering of sediment in glacial deposits found that clasts of leucocratic granite (which contain little or no biotite) rarely exhibit granular disintegration (45). In contrast grussification is much more common in the more biotite-rich clasts of granodiorite, tonalite, and quartz monzonite in the deposits (45). However, biotite concentrations were not measured in any of the clasts, so observations from the deposit only corroborate a connection between biotite presence and granular disintegration, not a connection between differences in biotite abundance (when it is present) and differences in weathering. Moreover, all of the mapped Inyo Creek bedrock is granodiorite and thus falls in the biotite-rich category that exhibited considerable weathering in the glacial sediment clasts (45).

Together, our observations from the field and a review of the literature provide little support for the possibility that differences in composition between Klp and the other two lithologic units could explain of the observed differences in sediment production and erosion across our study catchment. However, another possibility worth considering is that the differences in grain sizes of the minerals across the rock units help explain the observed differences in sediment production from slopes. Kw and Kp contain up to 10% large potassium feldspar phenocrysts, whereas Klp contains none. Nevertheless, the grain-size distributions of minerals are very similar overall between Kw and Klp, based on analyses of mineral sizes in bedrock from the outcrops shown in Fig. S3. Minerals in our sample of Kw were only slightly coarser than minerals in our sample of Klp, and the difference is only evident in the coarsest sizes (Fig. S3*E*). Upon complete granular disintegration, Kw might produce coarser sizes by virtue of lithology alone (irrespective of climate), but only in a mineral (K-feldspar) not analyzed geochemically or isotopically in this study, and only in a size that is present as a monomineralic grain in just the finer of the two creek-bed samples considered here.

Could the phenocrysts make it more likely for gravel-sized clasts to be produced by weathering on hillslopes underlain by Whitney Granodiorite, and thus explain the patterns we observe? To our knowledge, the influence of mineral grain size on the sizes of sediment produced on hillslopes has not been systematically investigated. However, a review of the literature on fracture mechanics yields some relevant insights. According to theory, larger mineral grain sizes tend to make brittle materials more susceptible to fracture (all else equal), because the grain boundaries act as flaws where fractures nucleate (48). Fracture toughness, which quantifies resistance to brittle fracture, scales with the inverse square root of flaw length. Thus theory predicts that measures of rock strength for various loading geometries (e.g., in compression, shear, and tension) also scale inversely with the mineral grain sizes. This has been confirmed in studies of bedrock and other brittle materials (49–52). Hence, one might expect bedrock with larger mineral grain sizes to be more susceptible to mechanical weathering (e.g., due to frost cracking and expansion of biotite) and thus might produce smaller, more numerous clasts of sediment. Based on this logic, the Whitney Granodiorite, with its large K-feldspar phenocrysts, should produce more fine sediment, in contrast to what our analysis indicates (Fig. 3). Either the difference in mineral grain size is too small to have an effect (Fig. S3), or the effects of climate and topography are large enough to overwhelm any effects of mineral grain size. Together, our new data on mineral grain sizes of the different rock units, and our review of the literature on fracture mechanics, suggest that the effects of differences in mineral grain sizes are too small to produce the patterns observed in Fig. 2.

The lack of connection between composition, mineral grain size, and the production of sediment across the catchment is underscored by qualitative observations of grain sizes both in channels and on catchment slopes. At our sampling point in the creek and on catchment slopes in the contributing area, Klp occurs in a wide range of sizes, from sand to boulders (Fig. S4). This indicates that the profound deficit in gravel over the 2000–2350 m elevation band (Fig. 3*A*, main article) is not entirely due to a higher intrinsic susceptibility to weathering of the underlying Klp bedrock. Klp can and does produce very coarse gravel (Fig. S4), but it does not do so in great abundance in the 2000–2350 m range, because erosion rates are slow enough and temperatures are high enough that few coarse gravel clasts are produced and delivered to the stream. Hence, climate and topography, not bedrock composition and mineral grain size, appear to be the key drivers of differences in sediment production across catchment slopes at Inyo Creek.

Fig. S4. Grain sizes produced on slopes and delivered to channels. (*Left*) Example of sediment on bed of Inyo Creek just downstream of ref. (12) 2002 sampling site. Scale: phone in image is 123-mm long. Arrows point to large and medium-sized clasts of Lone Pine Granodiorite (Klp). Note clast of Whitney Granodiorite at bottom of image with characteristic potassium feldspar phenocrysts. (Color contrast between dry light-colored clasts at left and wet, grayish clasts is due to moisture in creek, not staining from weathering.) (*Right*) Slope underlain by Klp in Inyo Creek catchment, illustrating that Klp breaks down into a wide range of sizes on slopes in the sediment contributing area.

Other Supporting Information Files

Datasets S1–S8 (eight worksheets in one .xlsx file)

1. PRISM Climate Group (2014) Climate Data. Available at: http://www.prismclimate.org.
2. Gillespie AR, Zehfuss PH (2004) in *Quaternary Glaciations - Extent and Chronology, Part II*, eds Ehlers J, Gibbard PL (Elsevier), pp 51–62.
3. Stone P, Dunne GC, Moore JG, Smith GI (2000) Geologic Map of the Lone Pine 15' Quadrangle, Inyo County, California. *US Geological Survey, Geologic Investigations Series I-2617*:1–1.
4. Farley KA, Wolf RA, Silver LT (1996) The effects of long alpha-stopping distances on (U-Th)/He ages. *Geochim Cosmochim Acta* 60:4223–4229.
5. House M, Farley KA, Stockli DF (2000) Helium chronometry of apatite and titanite using Nd-YAG laser heating. *Earth Planet Sci Lett* 183:365–368.
6. Farley KA (2000) Helium diffusion from apatite: General behavior as illustrated by Durango fluorapatite. *J Geophys Res* 105:2903–2914.
7. Shuster DL, Flowers RM, Farley KA (2006) The influence of natural radiation damage on helium diffusion kinetics in apatite. *Earth Planet Sci Lett* 249:148–161.
8. Flowers RM, Ketcham RA, Shuster DL, Farley KA (2009) Apatite (U–Th)/He thermochronometry using a radiation damage accumulation and annealing model. *Geochim Cosmochim Acta* 73:2347–2365.
9. Ruhl KW, Hodges K (2005) The use of detrital mineral cooling ages to evaluate steady state assumptions in active orogens: An example from the central Nepalese Himalaya. *Tectonics* 24:1–14.
10. Garver JI, Brandon MT, Roden-Tice MK, Kamp PJJ (1999) in *Geological Society, London, Special Publications*, eds Ring U, Brandon MT, Lister GS, Willett SD (Exhumation Processes: Normal Faulting, Ductile Flow and Erosion, London), pp 283–304.
11. Reiners PW, Ehlers TA, Mitchell S, Montgomery DR (2003) Coupled spatial variations in precipitation and long-term erosion rates across the Washington Cascades. *Nature* 426:645–647.
12. Stock GM, Ehlers TA, Farley KA (2006) Where does sediment come from? Quantifying catchment erosion with detrital apatite (U-Th)/He thermochronometry. *Geology* 34:725–728.
13. Vermeesch P (2007) Quantitative geomorphology of the White Mountains (California) using detrital apatite fission track thermochronology. *J Geophys Res* 112:1–11.
14. McPhillips D, Brandon MT (2010) Using tracer thermochronology to measure modern relief change in the Sierra Nevada, California. *Earth Planet Sci Lett* 296:373–383.
15. House M, Wernicke BP, Farley KA, Dumitru TA (1997) Cenozoic thermal evolution of the central Sierra Nevada, California, from (U-Th)/He thermochronometry. *Earth Planet Sci Lett* 151:167–179.
16. Kuiper NH (1960) Tests concerning random points on a circle. *P Koninklijke Nederlandse Akad Wentensch A* 63:38–47.
17. Press WH, Teukolsky SA, Vettering WT, Flannery BP (2007) *Numerical Recipes: The Art of Scientific Computing* (Cambridge University Press, Cambridge). 3rd Ed.
18. Granger DE, Riebe CS (2014) in *Treatise on Geochemistry*, ed Drever JI (Elsevier, Oxford), pp 401–436. 2nd Ed.
19. Granger DE, Smith AL (2000) Dating buried sediments using radioactive decay and muogenic production of Al-26 and Be-10. *Nucl Instrum Meth B* 172:822–826.
20. Granger DE, Kirchner JW, Finkel RC (1996) Spatially averaged long-term erosion rates measured from in situ-produced cosmogenic nuclides in alluvial sediment. *J Geol* 104:249–257.
21. Korschinek G et al. (2010) A new value for the half-life of ^{10}Be by Heavy-Ion Elastic Recoil Detection and liquid scintillation counting. *Nucl Instrum Meth B* 268:187–191.

22. Chmeleff J, Blanckenburg von F, Kossert K, Jakob D (2010) Determination of the Be-10 half-life by multicollector ICP-MS and liquid scintillation counting. *Nucl Instrum Meth B* 268:192–199.
23. Kohl CP, Nishiizumi K (1992) Chemical isolation of quartz for measurement of in-situ-produced cosmogenic nuclides. *Geochim Cosmochim Acta* 56:3583–3587.
24. Purdue University Department of Physics, ed. *Purdue Rare Isotope Measurement Laboratory* Available at: http://www.physics.purdue.edu/primelab/ [Accessed Jan 31, 2015].
25. Merchel S et al. (2008) Towards more precise ^{10}Be and ^{36}Cl data from measurements at the 10−14 level: Influence of sample preparation. *Nucl Instrum Meth B* 266:4921–4926.
26. Muzikar P, Elmore D, Granger DE (2003) Accelerator mass spectrometry in geologic research. *Geol Soc Am Bull* 115:643–654.
27. Nishiizumi K et al. (2007) Absolute calibration of 10Be AMS standards. *Nucl Instrum Meth B* 258:403–413.
28. Rossi B (1948) Interpretation of cosmic-ray phenomena. *Rev Mod Phys* 20:537.
29. Lal D (1991) Cosmic-ray labeling of erosion surfaces: In situ nuclide production rates and erosion models. *Earth Planet Sci Lett* 104:424–439.
30. Stone JOH (2000) Air pressure and cosmogenic isotope production. *J Geophys Res* 105:23753–23759.
31. Balco G, Stone JOH, Lifton NA, Dunai TJ (2008) A complete and easily accessible means of calculating surface exposure ages or erosion rates from Be-10 and Al-26 measurements. *Quat Geochron* 3:174–195.
32. Gosse JC, Phillips FM (2001) Terrestrial in situ cosmogenic nuclides: theory and application. *Quaternary Sci Rev* 20:1475–1560.
33. Dunne JA, Elmore D, Muzikar P (1999) Scaling factors for the rates of production of cosmogenic nuclides for geometric shielding and attenuation at depth on sloped surfaces. *Geomorphology* 27:3–11.
34. California Department Water Resources ed. *California Data Exchange Center* Available at: http://cdec.water.ca.gov [Accessed July 1, 2013].
35. Bierman PR, Steig EJ (1996) Estimating rates of denudation using cosmogenic isotope abundances in sediment. *Earth Surf Proc Land* 21:125–139.
36. Brown ET, Stallard RF, Larsen MC, Raisbeck GM, Yiou F (1995) Denudation rates determined from the accumulation of in situ-produced Be-10 in the Luquillo Experimental Forest, Puerto-Rico. *Earth Planet Sci Lett* 129:193–202.
37. Hirt WH (2007) Petrology of the Mount Whitney Intrusive Suite, eastern Sierra Nevada, California: Implications for the emplacement and differentiation of composite felsic intrusions. *Geol Soc Am Bull* 119:1185–1200.
38. Reiners PW, Thomson SN, McPhillips D, Donelick RA, Roering JJ (2007) Wildfire thermochronology and the fate and transport of apatite in hillslope and fluvial environments. *J Geophys Res* 112:1–29.
39. Woolfenden WB (2003) A 180,000-year pollen record from Owens Lake, CA: terrestrial vegetation change on orbital scales. *J Geophys Res* 59:430–444.
40. Matmon A et al. (2003) Erosion of an ancient mountain range, the Great Smoky Mountains, North Carolina and Tennessee. *Am J Sci* 303:817–855.
41. Belmont P, Pazzaglia FJ, Gosse JC (2007) Cosmogenic 10Be as a tracer for hillslope and channel sediment dynamics in the Clearwater River, western Washington State. *Earth Planet Sci Lett* 264:123–135.
42. Wahrhaftig C (1965) Stepped topography of southern Sierra Nevada, California. *Geol Soc Am Bull* 76:1165–1189.
43. Eggler DH, Larson EE, Bradley WC (1969) Granites Grusses and Sherman Erosion Surface Southern Laramie Range Colorado-Wyoming. *Am J Sci* 267:510–522.
44. Isherwood D, Street A (1976) Biotite-Induced Grussification of Boulder Creek Granodiorite, Boulder-County, Colorado. *Geol Soc Am Bull* 87:366–370.
45. Bustin RM, Mathews WH (1979) Selective Weathering of Granitic Clasts. *Can J Earth Sci* 16:215–223.
46. Buss HL, Sak P, Webb S, Brantley SL (2008) Weathering of the Rio Blanco quartz diorite, Luquillo Mountains, Puerto Rico: Coupling oxidation, dissolution, and fracturing. *Geochim Cosmochim Acta* 72:4488–4507.
47. Riebe CS, Granger DE (2013) Quantifying effects of deep and near-surface chemical erosion on cosmogenic nuclides in soils, saprolite, and sediment. *Earth Surf Proc Land* 38:523–533.
48. Scholz CH (2009) *The Mechanics of Earthquakes and Faulting* (Cambridge University Press). 2nd Ed.
49. Knudsen FP (1959) Dependence of mechanical strength of brittle polycrystalline specimens on porosity and grain size. *J Am Ceram Soc* 42:376–387.
50. Brace WF (1961) Dependence of fracture strength of rocks on grain size. *Proceedings of the Fourth Symposium on Rock Mechanics* 99–103.
51. Kumano A, Goldsmith W (1982) An analytical and experimental investigation of the effect of impact on coarse granular rocks. *Rock Mech* 15:67–97.
52. Eberhardt E, Stimpson B, Stead D (1999) Effects of grain size on the initiation and propagation thresholds of stress-induced brittle fractures. *Rock Mech Rock Eng* 32:81–99.